AGU PUBLICATIONS

JGR

Journal of Geophysical Research: Atmospheres

RESEARCH ARTICLE

10.1002/2017JD027220

Key Points:
- Meteoric smoke particles are abundant inside mesospheric ice particles
- The size distribution of fragments of ice particles can be determined with an impact/Faraday cup probe
- The size distribution of fragments of mesospheric ice particles is directly connected to meteoric smoke particles

Correspondence to:
T. Antonsen,
tarjei.antonsen@uit.no

Citation:
Antonsen, T., Havnes, O., & Mann, I. (2017). Estimates of the size distribution of meteoric smoke particles from rocket-borne impact probes. *Journal of Geophysical Research: Atmospheres*, *122*, 12,353–12,365. https://doi.org/10.1002/2017JD027220

Received 29 MAY 2017
Accepted 1 NOV 2017
Accepted article online 3 NOV 2017
Published online 26 NOV 2017

©2017. American Geophysical Union. All Rights Reserved.

Estimates of the Size Distribution of Meteoric Smoke Particles From Rocket-Borne Impact Probes

Tarjei Antonsen[1], Ove Havnes[1], and Ingrid Mann[1]

[1]Department of Physics and Technology, University of Tromsø, Tromsø, Norway

Abstract Ice particles populating noctilucent clouds and being responsible for polar mesospheric summer echoes exist around the mesopause in the altitude range from 80 to 90 km during polar summer. The particles are observed when temperatures around the mesopause reach a minimum, and it is presumed that they consist of water ice with inclusions of smaller mesospheric smoke particles (MSPs). This work provides estimates of the mean size distribution of MSPs through analysis of collision fragments of the ice particles populating the mesospheric dust layers. We have analyzed data from two triplets of mechanically identical rocket probes, MUltiple Dust Detector (MUDD), which are Faraday bucket detectors with impact grids that partly fragments incoming ice particles. The MUDD probes were launched from Andøya Space Center (69°17′N, 16°1′E) on two payloads during the MAXIDUSTY campaign on 30 June and 8 July 2016, respectively. Our analysis shows that it is unlikely that ice particles produce significant current to the detector, and that MSPs dominate the recorded current. The size distributions obtained from these currents, which reflect the MSP sizes, are described by inverse power laws with exponents of $k \sim [3.3 \pm 0.7, 3.7 \pm 0.5]$ and $k \sim [3.6 \pm 0.8, 4.4 \pm 0.3]$ for the respective flights. We derived two k values for each flight depending on whether the charging probability is proportional to area or volume of fragments. We also confirm that MSPs are probably abundant inside mesospheric ice particles larger than a few nanometers, and the volume filling factor can be a few percent for reasonable assumptions of particle properties.

1. Introduction

The polar summer mesopause, located at ~80–90 km altitude, is the coldest region of the terrestrial atmosphere, with temperatures sometimes approaching 100 K (Lübken, 1999; Zahn & Meyer, 1989). The low temperatures allow for growth of nanoscale ice particles, despite the low water mixing ratio around the order of a few ppmv (Hervig et al., 2003; Murray & Jensen, 2010). Cloud phenomena like the visible noctilucent clouds (NLC) and polar mesospheric summer echoes (PMSEs) observed by radar are related to the presence of water ice particles. NLCs consist of particles, typically of sizes around some tens of nanometers (see, e.g., von Cossart et al., 1999; Baumgarten et al., 2008), large enough to scatter light effectively and therefore detectable by a variety of optical remote sensing methods. PMSEs are coherent radar echoes observable at frequencies from the HF to the UHF regime, which are controlled by smaller subvisual particles. Smoke and/or ice particles can effectively reduce the mobility of electrons and allow for persisting electron gradients created by neutral turbulence, which subsequently can produce Bragg scattering (see, e.g., Rapp & Lübken, 2004 for a review). Ice particles $\gtrsim 10$ nm become predominantly negatively charged due to the work function of ice making photoemission and photodetachment less effective than the collection of free electrons in the *D* layer ionosphere (Knappmiller et al., 2011). Because of the charge state of the particles, electrostatic rocket probes are one of the preferred tools for in situ measurements. The first unambiguous detection of mesospheric charged particles was done by Havnes et al. (1996) with the rocket-borne Faraday bucket detector DUSTY. Their measurements confirmed the existence of negatively charged particles but did not exclude the possible effect of large positively charged dust grains or particles of meteoric origin on the measured currents.

Although water ice can form homogeneously around the polar summer mesopause during periods of relatively sharp negative temperature gradients (Murray & Jensen, 2010; Zasetsky et al., 2009), homogeneous nucleation between water vapor and condensation nuclei of meteoric material is generally thought to be the dominant growth mechanism for creating large ice particles ($\gtrsim 1$ nm) (Gumbel & Megner, 2009; Reid, 1997; Rapp & Thomas, 2006). Meteoroids ablate at heights between 70 and 110 km, and the resulting vapor condenses into agglomerates with radii ~ 0.1 to ~ 2 nm, commonly named meteoric smoke particles (MSPs),

which can subsequently partake in the ice particle formation process (Hunten et al., 1980; Megner et al., 2006). Exactly how MSPs are embedded inside larger ice particles was unclear for a long time and is still not completely resolved. Mesospheric ice particles were initially considered to be pure ice or contain a single or few MSP nuclei (Plane, 2003; Rapp & Thomas, 2006). Through revisiting measurements done with DUSTY, Havnes and Næsheim (2007) found that MSPs are probably abundant inside NLC particles. Based on analysis of rocket measurements where a small dust detector recorded much higher currents than a larger similar probe placed on the top deck, Kassa et al. (2012) also concluded that secondary charge production can dominate impact detectors and that embedded MSPs would amplify the secondary charging. Satellite measurements (Hervig et al., 2012) later confirmed that mesospheric ice particles are likely to contain meteoric material. Due to the neutral air flow around rocket payloads, particles of sizes $\lesssim$ 2 nm are swept away in the shock front and direct detection of MSPs is difficult (Hedin et al., 2007). To deal with this problem, Havnes et al. (2014) developed a new rocket probe based on their earlier findings — the MUltiple Dust Detector (MUDD) — which aimed to detect MSPs by fragmenting large ice particles and releasing embedded smoke particles in the collision with a fragmentation grid. The first version of MUDD was launched successfully in July 2011 on the PHOCUS (Particles, Hydrogen and Oxygen Chemistry in the Upper Summer mesosphere) payload, and measurements yielded information on distribution of collision fragments. It was found that $\sim$ 70% of fragments are smaller than $\sim$1.2 nm, 20% between 1.2 and 10% larger than 1.6 nm, when assuming the charging probability of fragments is proportional to their mass. This latter work also estimated the volume filling factor of MSPs inside NLC particles to be between $\sim$0.05% and several percent, consistent with the findings of Hervig et al. (2012).

From the first flight of MUDD, it was argued that the size distribution of the collision fragments was proportional to, if not directly transferable to the size distribution of free MSPs. Simulations of fragment dynamics and evaporation inside MUDD have showed that this is a plausible assumption (Antonsen & Havnes, 2015). To obtain an absolute size distribution of MSPs from the MUDD detector, however, uncertainties in the charge transfer mechanism (i.e., triboelectric) during a collision between ice particles and the fragmentation grid must be resolved. Such charging mechanisms are not well understood for $\sim$ 1 nm particles in the mesosphere. Therefore, we rely on experimental work on pure ice particles (Tomsic, 2001) and meteoric analogues (Adams & Smith, 1971), along with theoretical considerations on the topic (Antonsen & Havnes, 2015; Havnes et al., 2014; Kuuluvainen et al., 2013). For nanoscale ice particles, the experiments showed that fragments have predominantly negative charge, up to a few minutes after bombardment on a clean metal surface. After the initial few minutes, a significant number of the fragments can become positively charged. We assume for this reason that the fragments are negatively charged in our simulations of fragments inside MUDD.

In the present study, we aim for a higher resolution in MSP sizes and of the spatial variation of dust/ice layers around the mesopause compared to the 2011 flight of MUDD. Due to technical difficulties (i.e., electrometer settling) there is a trade-off between size and height accuracy in a single probe. We therefore use three mechanically identical probes with partially overlapping detection modes (voltage biases), so that a large part of the mass spectrum can be covered while probes can be referenced to each other continuously to make recalibration of the instruments more convenient.

In section 2 we present the new version of the MUDD dust detector. Section 3 presents the measurements obtained by, and technical details of, two triplets of MUDD probes on two sounding rocket launches, MAXIDUSTY 1 (MXD-1) and MAXIDUSTY 1B (MXD-1B), during the summer of 2016. In section 4 we present and discuss the size distribution of collision fragments of mesospheric ice particles detected by MUDD and their relation to MSP size spectra. In section 5 we give a short summary, discussion, and concluding remarks on the results.

2. The New MUltiple Dust Detector — MUDD

A cross section of MUDD is shown in Figure 1. The MUDD probe is a Faraday bucket-type detector with two statically biased grids and a bottom plate detector varying between four different voltage biases sequentially. The shielding grid, G0, is set to the floating payload ground and shields neighboring instruments from interior electric fields. The positive ion shielding grid, G1, is biased to +6.2 V, which is sufficient to shield from the positive ambient species. The fragmentation grid, G2, consists of inclined rings that partly overlap to prevent the direct influx of large ice particles to the bottom plate. An ice particle with a radius around 50 nm will be partially fragmented at impact with G2 and normally produce between 50 and 100 charged fragments,

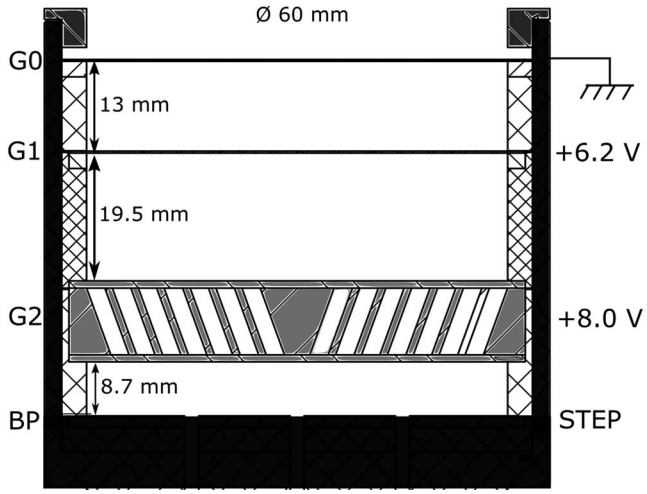

Figure 1. Principle sketch of the MUDD detector. The G0, G1, and G2 grids have a constant bias, while BP steps between different voltages to produce the retarding potentials for detection of particles of different sizes. A single MUDD probe has three unique voltage modes and one mode that overlaps with one of the other probes for comparison and calibration.

depending on the radius proportionality of the triboelectric charging of the fragments (Havnes & Næsheim, 2007). The fragments will subsequently travel toward the bottom plate (BP), almost parallel with the G2 planes, with an energy of around 40% of the initial energy (Antonsen & Havnes, 2015; Havnes et al., 2014; Tomsic, 2001).

On two separate payloads, MAXIDUSTY 1 and MAXIDUSTY 1B, identical triplets of MUDD were launched. The probe layout on the payload top deck for the MXD-1B payload is shown in Figure 2. The top deck geometry was identical to the one of the MXD-1, apart from the UC Boulder instrument miniMASS (mini Mesospheric Aerosol Sampling Spectrometer) that substituted DUSTY 1 on the first flight. The electrostatic dust probe measurements were supported by boom probe measurements of electron density; both by Faraday rotation (Jacobsen & Friedrich, 1979) and multineedle Langmuir probes (Bekkeng et al., 2010; Jacobsen et al., 2010). A new mass spectrometer, ICON (Identification of the COntent of Noctilucent cloud particles) (Havnes et al., 2015), was included on both payloads to analyze the chemical composition of NLC particles. The three MUDD probes had four unique voltage steps totaling to 10 different voltage modes, that is, two overlapping voltage modes for referencing and calibrating probes relative to each other. The respective voltage modes of each of the MUDDs are listed in Table 1, in terms of retarding potential for negatively charged fragments. A negative retarding potential implies attracting forces for negatively charged fragments. The potentials were chosen on the basis of the extensive modeling and experimental results of Antonsen and Havnes (2015) and Havnes et al. (2014), respectively, such that a large part of the theoretical size distribution is covered. Positive retarding potentials will stop all fragments up to a certain size, and the raw current of a single channel will correspondingly represent a cumulative distribution. By subtracting bins of higher retarding potential, an absolute distribution can be obtained. We have also included a mode in which all negative fragments will be attracted to the bottom plate ($U_R = -2$ V), even down to a couple of Ångstrøms in size, to yield a higher sensitivity in the lowest part of the size spectrum (which is thought to contain the highest number of particles) and a more correct total current.

The currents to G1, G2, and BP were sampled at a rate of 8,680 Hz, and the voltage modes switched every 192 samples (~15 m in altitude around the mesopause). The three probes ran in parallel with identical sampling rates, but with a 64-sample interval between the first voltage mode in each group, such that the first voltage mode of MUDD-2 started 64 samples after the first mode in MUDD-1 and so on. This means that in every full cycle (four voltage modes) MUDD-1 overlapped with MUDD-3 in the −2 V retarding mode for 64 samples (~6 m); correspondingly, MUDD-2 overlapped for the same number of samples with MUDD-3 in the +8 V mode. The stepping scheme of the potentials for the different probes is illustrated in Figure 3.

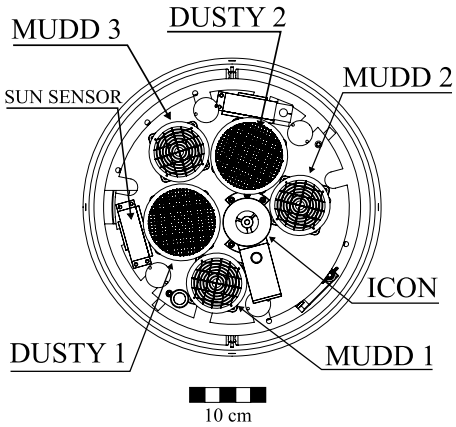

Figure 2. Top deck layout on the second MAXIDUSTY payload. The MUDD and DUSTY probes are the Faraday buckets from UiT. The first payload was mechanically similar but with one of the DUSTY probes replaced with the UC Boulder miniMASS.

3. MUDD Observations During the MaxiDusty Campaign

Two triplets of MUDD probes were launched from Andøya Space Center (69.29°N, 16.02°E) at 09:43 UT on 30 June 2016 and 13:01 UT on 8 July 2016, respectively, on the MXD-1 and MXD-1B sounding rocket payloads. MXD-1 was launched through a relatively broad NLC, reaching from ~80 to 86 km, as detected by the RMR-lidar at the ALOMAR observatory (see Gerding et al., 2016; Von Zahn et al., 2000 for technical details). This NLC had a strong volume backscatter coefficient from 80 to 82 km and a more diffuse appearance in the upper part. Observations of PMSE were made simultaneously and in the same volume as the rocket path by the MAARSY radar during the entire campaign. The PMSE structure during the MXD-1 launch, as shown in Figure 4, was highly dynamic with moderate echo strength. At the time of launch, the PMSE stretched from around 80 to 90 km in a nonhomogenous structure. The radar beam along the rocket flight path showed that the payload passed through three moderately strong PMSE layers but missed

Table 1
Voltage Modes of the MUDD Probes in Terms of Retarding Potential in Volts

Probe	Ret. Potential (V)
MUDD-1	(−2, 0, 2, 4)
MUDD-2	(13, 18, 5, 8)
MUDD-3	(−2, 1, 3, 8)

the regions of strongest backscatter. For the MXD-1B launch, clouds obscured the NLC measurements, but PMSE backscatter from the height region between ∼ 84 km and ∼ 88 km was very strong and appeared relatively homogeneous in comparison to the PMSE from the first launch.

3.1. MUDD Measurements on MXD-1

The analysis of the raw MUDD currents requires some in-depth explanation. Due to the settling time of the MUDD electrometers after switching between voltage modes, the first 10–20 samples in every voltage step (192 samples in total) cannot be directly used. To be certain of minimizing the effect of electrometer settling, we removed the 20 first samples in every voltage step for all potential modes. For most of the potential modes, a weak settling could still be observed after the removal of the initial 20 samples. The remaining 172 samples of all voltage steps were consequently fitted with an exponential function in region with no dust (example shown in Figure 5a), and the slow settling components were subtracted.

Furthermore, an issue with electron current leakage must be resolved. Ideally, no electron current would be measurable on the bottom plate for all retarding potential modes. This implies in theory that only the $U_R = -2$ V and $U_R = 0$ V could show signs of ambient electrons reaching BP, since these modes do not retard negative particles. In reality, due to the complex E field structure inside MUDD and other possible effects such as payload charging, minor current contributions from ambient electrons are present for retarding potential modes up to ∼ 5 V. In these cases, currents from the regions 79 km to 81 km (below NLC) and 86.7 km to 90 km (above NLC) were fitted by cubic polynomials to a very good agreement. An example of the fitted curves for one of the MUDD probes is shown in Figure 5b, where we note that the voltage mode with $U_R = 8$ V does not require background subtraction. Such a fitting procedure is valid when there is no clear bite-out in the G2 current and does not require an iteration process as employed in Havnes et al. (2014). For the PHOCUS payload, the least retarding channel had $U_R = 10$ V and electron leakage was only observed in the zero potential mode, which agrees with the MXD-1 results.

Figure 6 shows the recorded upleg currents of G1 and G2 for MUDD-1. The same channels for the other two probes in the MUDD triplet show almost identical current strengths and features. The spike at ∼83.5 km is due to the firing of a squib on the ICON instrument, also situated on the top deck. Both of these channels display a spin modulation of 3.8 Hz, which is expected for G1 and also for G2 whenever secondary particles produced at G1 or the probe walls hit the lower grid. This modulation was removed in postprocessing, as discussed later. We note that no clear electron bite-out was observed by MUDD; although a slight tendency of a weakening of the negative dust current may be seen, in contrast to the 2011 flight on the PHOCUS payload (Havnes et al., 2014). The Faraday rotation electron density probes and mNLP Langmuir probes on MXD-1 observed a strong bite-out for a background electron density of ∼ $10^9 \mathrm{m}^{-3}$, with two pronounced peaks at 83 km and 86 km (M. Friedrich and E. Trondsen, private communication, 2017). This confirms that the ice particles residing in the NLC were predominantly charged negatively.

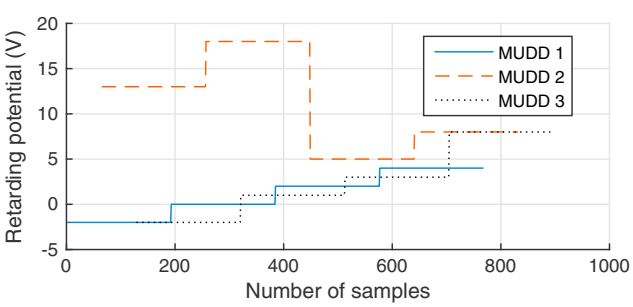

Figure 3. Stepping scheme of the different retarding potential modes for all MUDD probes. Note that the modes are slightly shifted in time relative to each other and the overlap between probes at $U_R = -2$ V and $U_R = 8$ V. The sampling frequency is 8,680 Hz, implying that a group of four steps, or 768 samples, takes ∼0.09 s to complete.

The bottom plate currents from MaxiDusty-1 are shown in Figure 7. The noise due to the squib firing at 83.5 km is present also in this data. Currents for equal voltage modes from the different probes, as well as evolution with altitude, match very well. The calibration factor between probes is addressed below. The regions where BP currents show clear signs of dust fragments matches with the lidar backscatter from the NLC; however, the PMSE strength does not follow the bottom plate current well, especially in the upper part of the echo. The currents above ∼86 km are weak, apart from a few short scale signatures on the order of ∼10 m. From the combined remote measurements and MUDD currents we shall therefore assume that there resided a population of relatively large ice particles in two layers: up to 84 km and around 85 km. Preliminary calculations of NLC particle sizes from RMR-lidar and the onboard photometer from the Department of Meteorology at Stockholm University also support this assumption (G. Baumgarten and J. Hedin, private communication, 2017). Further analysis of the DUSTY results confirms this. A population of smaller (PMSE) ice particles were probably present throughout the height region between 81 and 86 km.

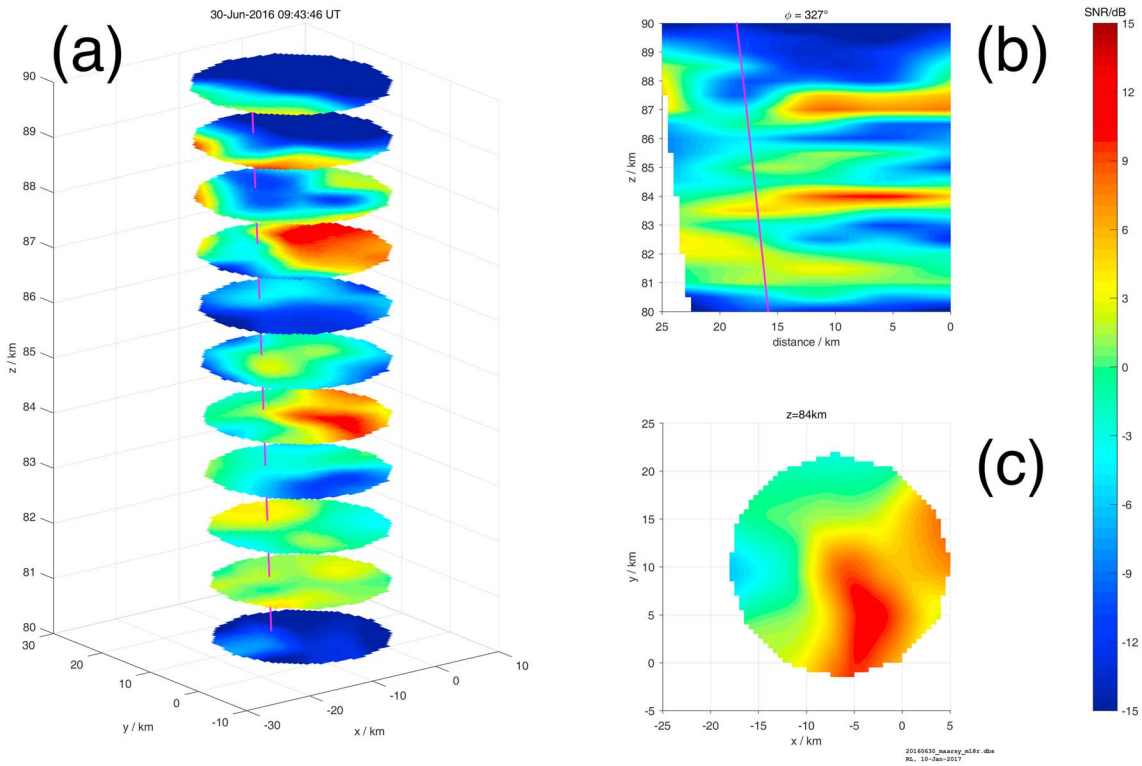

Figure 4. PMSE profile along rocket trajectory (marked as solid line) obtained with MAARSY for the MXD-1 flight. (a) Two-dimensional slices with a radius of 10 km, throughout the region containing PMSE. (b) A vertical slice in the plane of the rocket trajectory. (c) A two-dimensional snapshot of the PMSE at 84 km. Courtesy of Dr. Ralph Latteck, IAP Kühlungsborn.

The recorded BP currents increase with decreasing retarding potential, and the attracting mode $U_R = -2$V consistently records the strongest currents. For the neighboring modes $U_R = 1$ V and $U_R = 2$ V, the latter gives a bigger contribution to the total raw current; however, the effective current is still smaller when taking charging probability into account, as will be discussed below.

We must also address the calibration of the probes. MUDD-1 and MUDD-2 are, as mentioned above, referenced to MUDD-3 at potential modes $U_R = -2$ V and $U_R = 8$ V, respectively. For further analysis, we recalibrate the probes to MUDD-3 in the overlapping potential modes and use the same calibration factor for all potential modes. Using the same calibration is analogous to assuming that the dusty plasma has no fluctuations on length scales comparable to the payload diameter. This should most often be the case since the power spectral

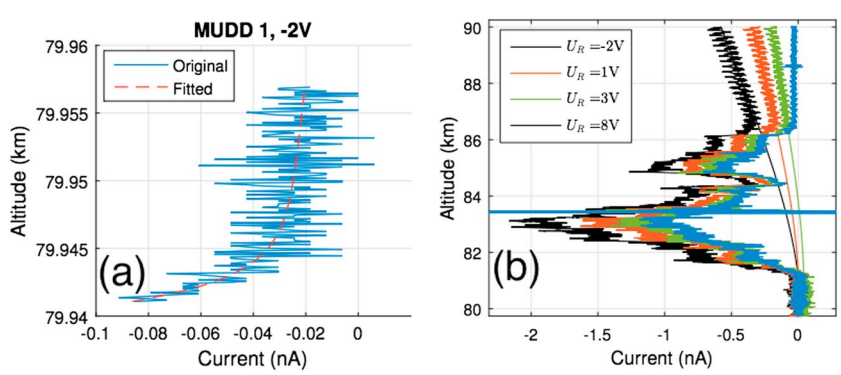

Figure 5. Steps in the postflight preparation of MUDD data. (a) Varying current in a single voltage mode when there is no dust, due to electrometer settling. The 20 first samples of the group have been removed, such that the length is 172 samples. (b) Changing BP current with height due to leakage electron current. Both these effects are removed by fitting and extracting fitted curves.

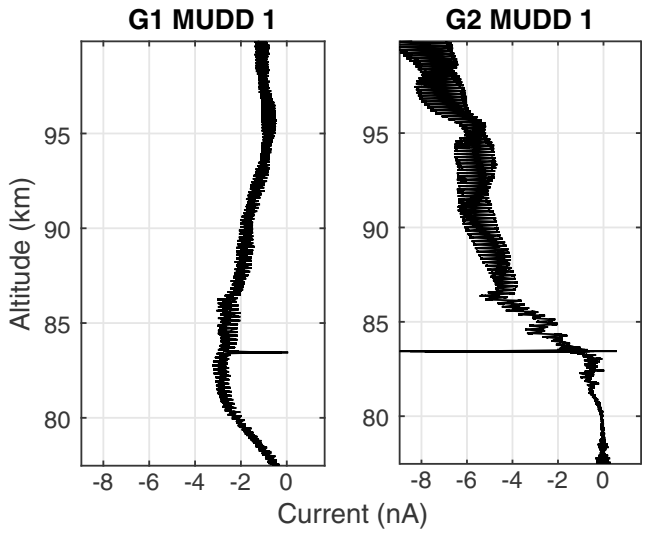

Figure 6. Raw currents to shielding grid (G1) and fragmentation grid (G2) from MUDD-1 on MXD-1. A bite-out in the electron population can be inferred by the G1 currents. The sharp peak around 83.5 km is due to a squib firing.

density in the neutral gas, for which the dusty plasma is a passive tracer, normally decreases rapidly at length scales less than a few meters (Rapp & Lübken, 2004). The payload diameter is 0.356 m. Figure 8 shows the two calibration factors through the ice layer for the MXD-1 flight. The probe currents are chosen as the median value for each voltage step of 172 samples, to reduce noise from very short current fluctuations. The ratio is close to unity throughout the whole layer with the exception of the height region near the squib firing at ~ 83.5 km and the very rapid change in current at ~ 84.2 km. A weak variation due to spin modulation is also observed. In the calculation of the total current contribution from the different potential modes, we have utilized the median value of every voltage step and rescaled the all currents according to the calibration curves in Figure 8.

3.2. MUDD Measurements on MXD-1B

The data handling and analysis procedures of the MXD-1B MUDD data are identical to the procedures utilized on MXD-1 data described in the previous section. Although the probe settings on the two payloads were identical, the recorded MUDD currents from the MXD-1B flight are difficult to explain with — or compare to — the previous MUDDs and also other Faraday bucket probes. For MXD-1, MUDD records currents that can be expected when the ice population consists of a significant number of large particles. This was also confirmed by DUSTY measurements for MXD-1, by employing methods used in several earlier works to characterize the charged particle population (see, e.g., Havnes & Næsheim, 2007; Havnes et al., 1996). For MXD-1B, all G1 and G2 grids on MUDD probes show very large negative currents but only a relatively weak bite-out and with heavy spin modulation even though attitude measurements show very little coning. The BP currents also behave unexpected but consistently with the G1 and G2 currents shown in Figure 9. These very negative currents are also seen in the two DUSTY probes flown on MXD-1B, for which we at present time do not have one single plausible explanation. The unusual signatures from the Faraday buckets on MXD-1B will be the topic of future work. Due to the highly variable currents, the calibration factor for MXD-1B is also variable and deviates significantly from unity at certain altitudes, as shown below. There is, however, little doubt that parts of the dust layer contain the typical ice particles as observed during the MXD-1 launch, and the results derived from MXD-1B data should to a certain degree yield valid estimates of fragment sizes. A natural consequence of the high variance is that the error becomes larger in the fitted size distribution.

Figure 10 shows all the raw bottom plate (BP) currents for the MXD-1B flight after subtraction of the electron leakage contribution. The altitude profile follows the shielding and fragmentation grid currents fairly well,

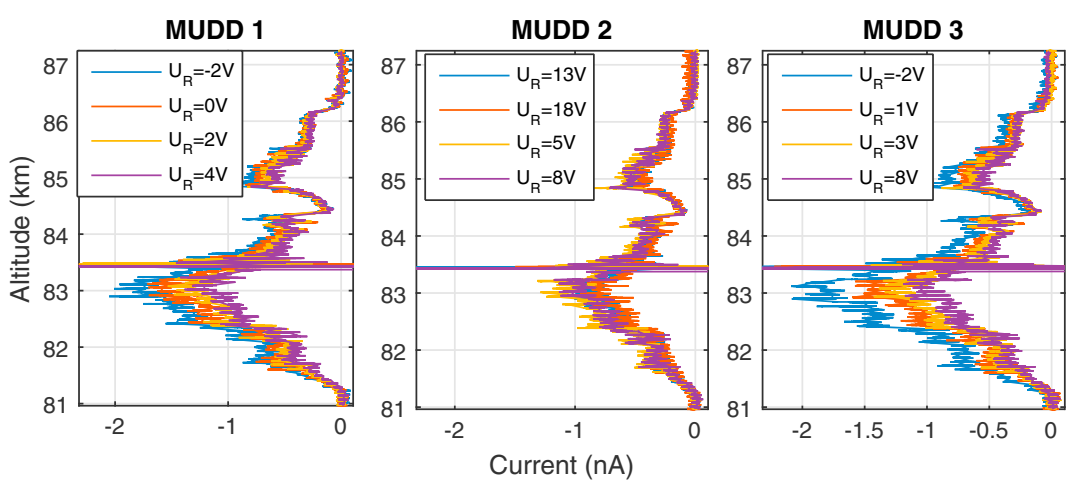

Figure 7. Raw currents corrected for increasing leakage electron current from the BP channel of all the MUDD probes on MXD-1.

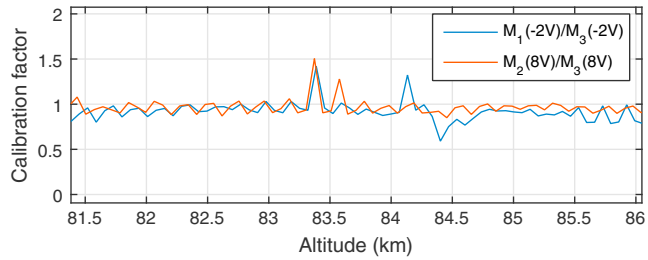

Figure 8. Calibration factor for equal potential modes on different probes. The probes are calibrated in flight by the ratio of overlapping potentials between probes. For MUDD-1 and MUDD-3 (blue line), the overlapping modes had retarding potential $U_R = -2$ V. For MUDD-2 and MUDD-3 (red line), the $U_R = 8$ V modes overlapped.

but a closer inspection reveals that structures are not completely coincident. This points toward a complicated relationship between the ambient dusty plasma parameters that cannot be resolved through analysis of the MUDD probes alone. Instrumental effects such as payload charging cannot be ruled out, but analysis of the floating potential of the onboard Langmuir probes (E. Trondsen, private communication, 2017) probably cannot explain the profile. It can also be speculated that UV radiation can affect the recorded current. The ~ 3.8 Hz spin modulation is prominent in the dust structure in the middle, however not as visible in the lower and upper layers. In general, the MXD-1B flight lacks the characteristics typical of large secondary charging effects where the current to G2 can become partly positive in the DUSTY probe. This would be a clear confirmation that a fragmentation charging process is dominating the G2 current and significantly influences BP currents.

The in-flight calibration curve, as discussed above, is shown in Figure 11. This deviates from the ideal situation where both curves are close to unity.

It is a likely possibility that the PMSE is partly populated by high concentrations of very small ice particles, many of which can be uncharged but may severely influence on the payload potential, by scavenging electrons from its surface. Artificial variations in the currents to the dust probes may also occur due to the airstream around the payload affecting smaller incoming particles. The deviation is only present for MUDD-1B, which has the lowest retarding potentials. A possible explanation is that the irregularity originates from a relatively high concentration of small charged ice particles with radii of a few nanometers that are barely energetic enough to penetrate G1 down to G2, but not further. However, the difference between equal potential on different probes cannot easily be explained. Another possible explanation of a calibration factor of ~10 could be that one of the booms measuring electron density (mNLP) was stuck in a (partly) vertical position such that the payload top deck was sprayed with fragments during certain periods of the rotation (Friedrich, private communication). Nevertheless, the fragment currents are stronger in the height region from 85.5 km to 86.7 km for all probes, and in the further analysis we use this region but recalibrate the currents for MUDD-1B.

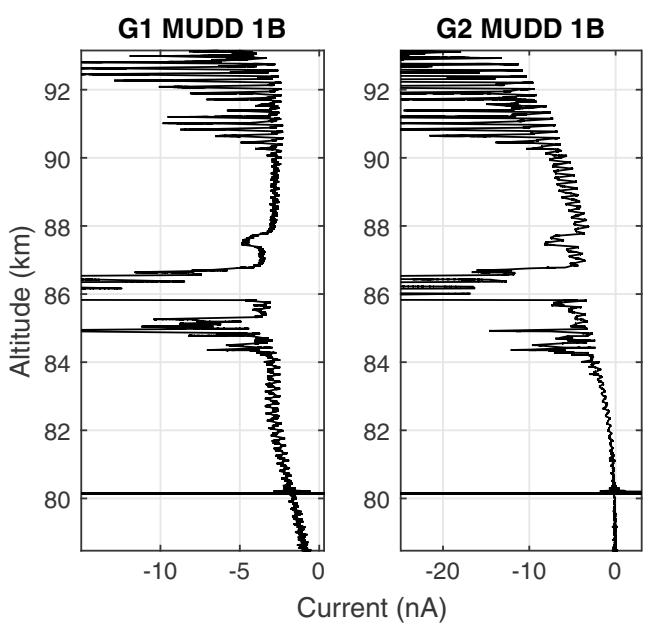

Figure 9. Raw currents to shielding grid (G1) and fragmentation grid (G2) from MUDD-1B on MXD-1B. The G1 current is more dynamic than on the first flight, but a bite-out can still be inferred from the profile. The peak at ~ 80 km is due to a squib firing.

4. Derived Size Distributions of Collision Fragments

Each potential step is 192 samples long (in the raw form), which corresponds to ~17.5 m along the payload orbit within the ice layer. Relatively large fluctuations on length scales smaller than this can readily occur, and we therefore utilize the median of each potential step when calculating a mean size distribution. With this method we obtain 10-point mean size distributions with an altitude resolution of ~ 70 m. Due to the internal mechanical structure of MUDD not being perfectly axisymmetric—for example, two cross beams strengthening G2—there is also spin modulation present in the BP currents. This effect was reduced by Fourier transforming and attenuating the 3.8 Hz frequency bins and the pronounced harmonics.

Currents from within the ice layer from the three MUDD probes on MXD-1, normalized to the $U_R = -2$ V mode, are shown in Figure 12. When two probes measure in the same mode simultaneously, an average of the currents is used. As confirmed by the raw currents, less retarding potential modes observe larger currents more or less consistently, as expected. An interesting feature is that the normalized contribution from the lower potential modes decrease with altitude, while higher retarding potentials record relatively larger currents. In multilayered dust clouds, it is possible that respective layers can have certain differences in size distributions, but even with homogeneity there are a few different possible explanations for this observed feature.

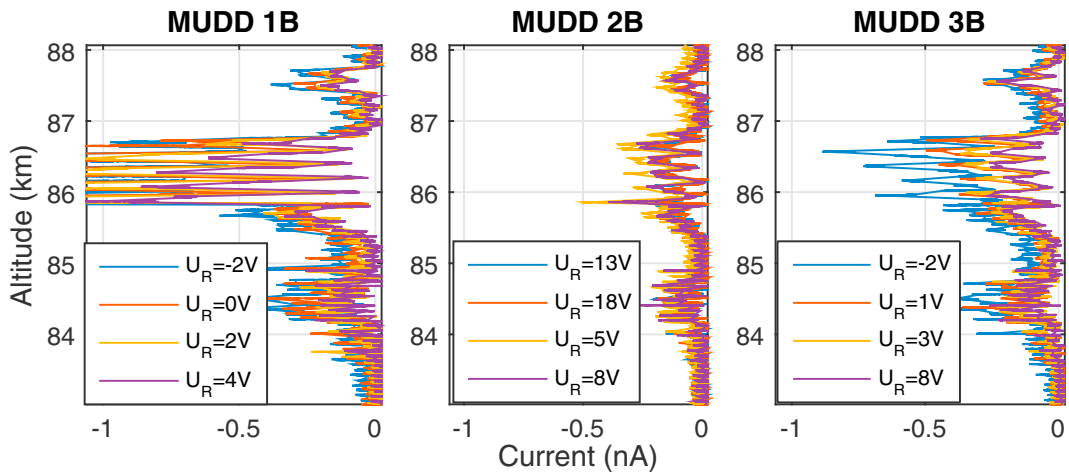

Figure 10. Raw currents corrected for increasing leakage electron current from the BP channel of all the MUDD probes on the MXD-1B payload.

Larger fragments topside. The variation in current with potential may be interpreted as fragments being larger at the topside of the dust cloud, which would be opposite from what is expected. However, this is unlikely in both of the main models of the mesospheric ice particle. First, if the large ice particles are solely made up of pure water ice throughout the cloud, this indicates that ice fragments increase in size with altitude. A physical description of such a situation cannot be obtained easily. Second, if the fragment size distribution is directly linked to the MSP size distribution, it would require that MSPs increase in size with altitude—opposite from what one would expect from growth and sedimentation mechanisms.

Changing production factor. Alternatively, the narrowing of the response versus potential with height in Figure 12 could indicate that the production factor of fragments decreases with altitude, which is consistent with the lidar measurements indicating fewer and/or smaller ice particles on the topside of the dust layer. Larger particles at the bottom would have more kinetic energy available to partly break the ice particle upon impact with the G2 grid and probably produce more fragments. We do not expect a strong influence on the MXD-1 observations due to particle sedimentation into warmer regions, since temperature measurements with iron lidar recorded consistent low temperatures $\sim$ 120 K throughout the whole region (J. Höffner, private communication, 2017). Also, the changing rocket speed throughout the layer will probably add to the effect. For MXD-1 the rocket velocity is approximately 838 m s^{-1} at 81 km and 772 m s^{-1} at 86 km, yielding a $\approx$ 15% reduction in impact energy at G2. This conclusion is also supported by mass spectrometer measurements indicating that the topside of the layer contains smaller particles, possibly free MSPs, which would not enter MUDD (Robertson et al., 2009).

"Nanodust shedding" effect. As a third explanation, we must mention a recent development in charging mechanisms for mesospheric nanoparticles that may explain a possible physical mechanism, where larger MSPs can be more abundant in the fragment distribution at the top of a NLC/PMSE layer. In a recent work, Havnes and Hartquist (2016) proposed a new mechanism where MSPs can scavenge electrons from larger ice particles (so called "nanodust shedding") that can further affect the internal distribution of MSP sizes inside ice particles. The physical explanation is that the switching time of the polarized ("image") potential on the surface of an ice particles is *slow* compared to the charging and escape rate of an impinging MSP. The result is that small MSPs are effectively shed, and large ice particles contain an overrepresentation of relatively large MSPs. The effect is stronger for low neutral temperatures ($\lesssim$ 120 K, which was the case for MXD-1, as measured by iron lidar; Höffner, private communication). Near the top layer of the dust cloud, the number density of the larger NLC particles may be low enough for the nanodust shedding effect to effectively quench the sticking of the smallest MSPs to the ice particle surface. In the lower part of the ice cloud, the number

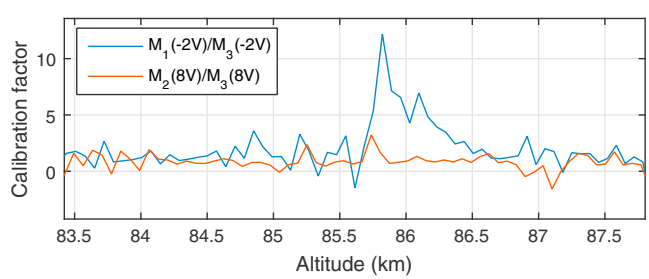

Figure 11. Calibration factor for equal potential modes on different probes for MXD-1B. The relatively high correction suggested by the ratio of the $U_R = -2$ V modes (blue line) is discussed in the text.

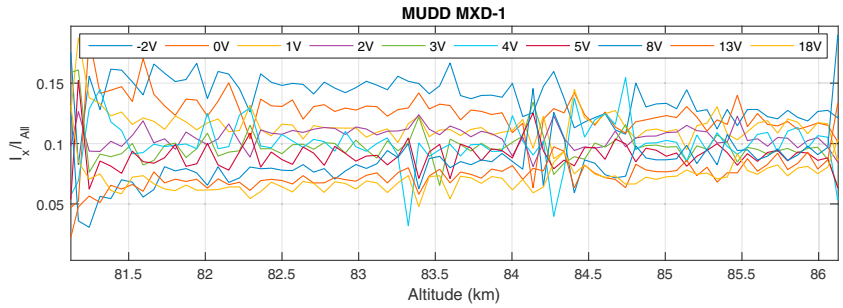

Figure 12. Ratio between MUDD currents from each retarding potential channel, respectively, (I_X) and the sum of all currents (I_{All}), that is, relative contribution to the total current, on the MXD-1 payload.

densities are high enough to absorb a large proportion of smoke particles, regardless. The shedding effect is suggested to affect short time scale charging events but depends on many intrinsic parameters that introduce uncertainties.

The normalized currents from the dust layer centered at ~ 86.5 km during the MXD-1B launch are shown in Figure 13. The trend with decreasing currents with altitude, as seen during MXD-1, can be observed also here. The arguments given above for this observed trend should be valid for both flights. We note that the attracting channel current ($U_R = -2$ V) is comparatively larger for MXD-1B, and that the analyzed height region is much shorter for the second flight.

To obtain the fragment size distribution from the MUDD currents, we need to determine the true current contribution of fragments. Without knowing the size distribution of the incident particles that produce the fragments, it may be difficult to get accurate estimates of how the fragment size distribution develops with altitude (cf. the discussion above). We therefore calculate the integral contribution of all modes to yield a mean fragment size distribution throughout the dust layer. Figure 14 shows the integrated but otherwise untreated current distribution normalized to the current of the $U_R = -2$ V mode. In this distribution, all different potential modes contain currents from modes of higher retarding potentials, which need to be removed. For some neighboring bins, the mode with the highest retarding potential observes larger current than the lower potential mode. This may seem unphysical, but we note that the charging probabilities of fragments are not taken into account here and must be included to yield a correct size distribution.

To obtain the general size distribution we need also to calculate what fragment sizes correspond to each retarding potential and their respective charge state. The problem of relating the MUDD currents to fragment sizes was treated in depth by Antonsen and Havnes (2015). In that work, the movement inside MUDD of both pure MSPs and MSPs coated with ice layers of different thicknesses was simulated, and it was found that the recorded currents at BP (for the potential modes used here) are most likely from pure MSPs, rather than pure ice or a mixture of ice and meteoric material. In the present work we have utilized the dust dynamics model from the previously cited work and calculated the size bins for each potential mode. A short comment on a few

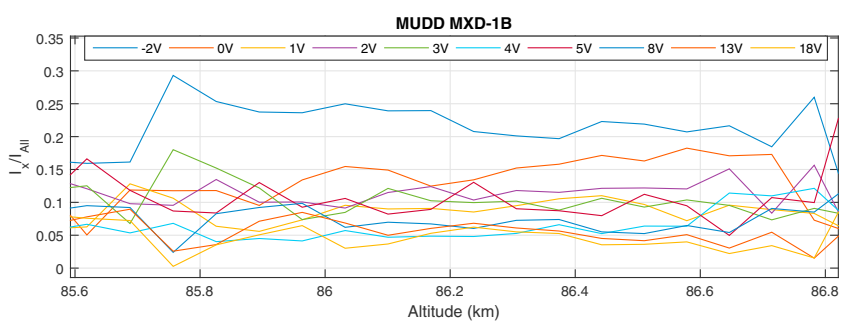

Figure 13. Relative contribution to the total currents for all retarding potential modes in the dust layer from 85 to 87 km on MXD-1B.

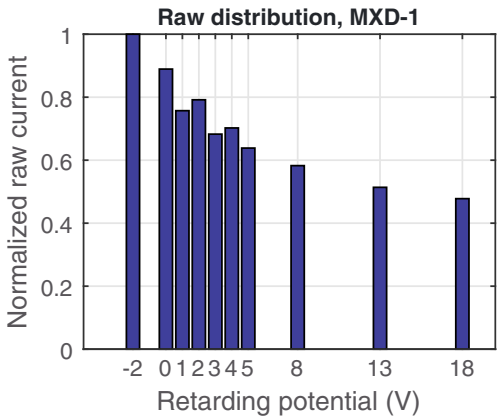

Figure 14. Distribution of integrated MUDD fragment currents from all channels of MUDD on MXD-1, corresponding to a cumulative mass distribution normalized to the current in the $U_R = -2$ V mode (total current, such that $I(-2V) = 1$). This is not adjusted for difference in charging probability.

central simulation parameters should be made. We have here assumed that 40% of the initial kinetic energy is preserved for movement of fragments, while the rest is dissipated to internal degrees of freedom in the fragmentation progress, that is, partial fragmentation, heating, and evaporation, as justified by experiments (Havnes et al., 2014; Tomsic, 2001). A change in the set initial fragment energy of ±10% then yields a difference in initial velocity of around ±50 m s^{-1}. The difference in estimates of the fragment size subsequently translates to roughly ±0.1 nm (Antonsen & Havnes, 2015). Furthermore, the MSP mass density is set to 3,000 kg m^{-3} (Klekociuk et al., 2005; Plane, 2011), and fragments are assumed to be singly negatively charged.

The charging probability of the fragmented dust particles introduces a relatively large uncertainty in the final mass distribution. The principal assumption to utilize for the charging state is that the charging probability is $P_c \propto m_{\text{frag}} \propto r^3$ for pure MSP fragments, following Friichtenicht (1964) and Adams and Smith (1971). This may not, however, be directly applicable to the case of relatively low velocity collisions. The dominating charging mechanism is triboelectric, so that we have also included the possibility of $P_c \propto r^2$, which should be a probable scaling. The obtained final size distribution, shown in Figures 15a and 15b for the first launch and Figures 15c and 15d for the second launch, shows similar trends as the theoretical distributions of free MSPs of Bardeen et al. (2008), Hunten et al. (1980), and Megner et al. (2006) (at 90 km), with the size range, 0.45–1.5 nm, spanning about 2 orders of magnitude in concentration. The theoretic distributions

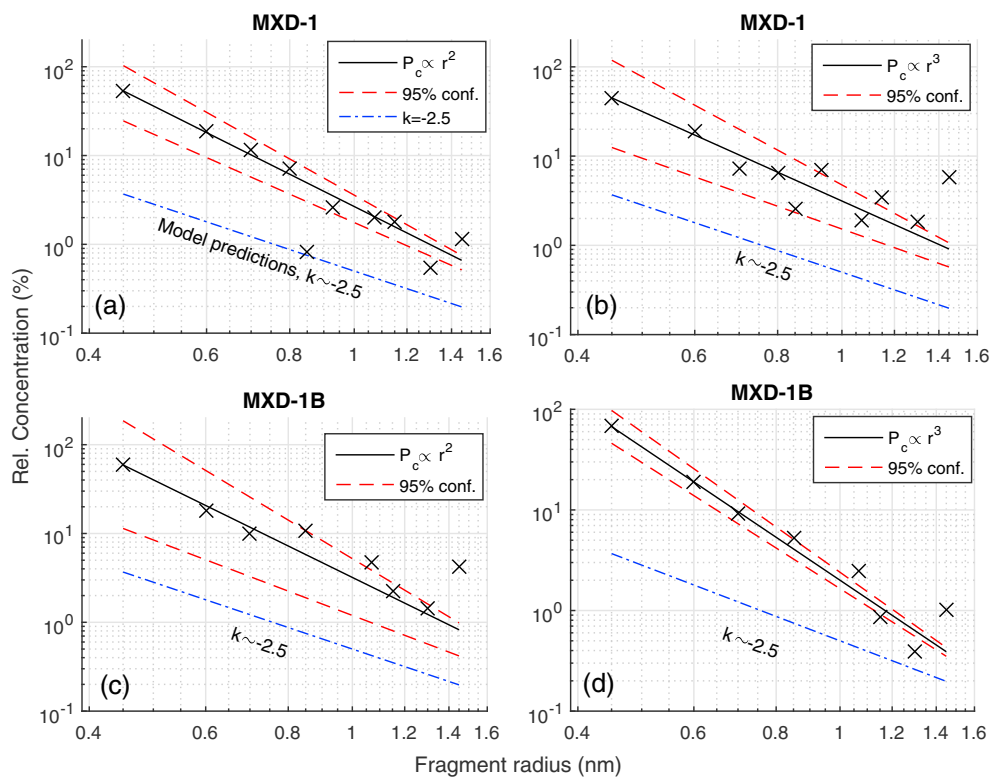

Figure 15. Obtained size distributions of collision fragments (MSPs inside ice particles) in MUDD on the MaxiDusty payloads for limiting values of charging probability (P_c). The obtained distributions are plotted as solid black lines, while the 95% confidence bounds are plotted in red dashed lines. The blue dash-dotted lines shows a fit of modeled size distributions of free MSPs at 90 km based on Bardeen et al. (2008), Hunten et al. (1980), and Megner et al. (2006). We note that the model prediction fit have been shifted down to emphasize the gradient; that is, the relative concentration is not accurate. (a) The MXD-1 case for P_c proportional to the fragment cross section. (b) The MXD-1 for P_c proportional to fragment volume. (c and d) The same respective limits of P_c for the MXD-1B flight.

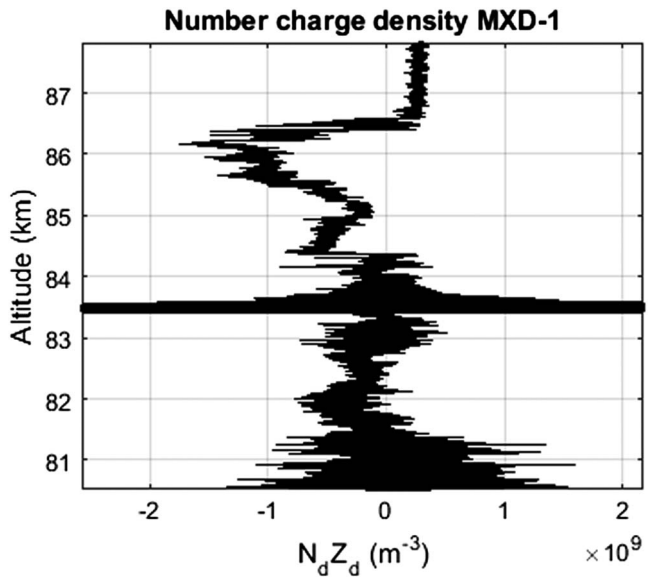

Figure 16. Charge number density throughout the layer containing dust/ice particles during MXD-1 derived from the DUSTY probe. The noisy nature of the profile around 83.5 km and below 81 km is due to mechanical stress from squib firings.

presented in the three modeling papers, plotted in blue dash-dotted lines, agree very well in the size range detectable in MUDD and a mean fit is presented. We note that the theoretic MSP distributions around 90 km can have a dependence on the production curve for meteoric ablated material, and some variation can be expected. If we look closer at the inverse power law size distributions that arise from the different charging probabilities, $n(r) \propto r^{-k}$, the exponent for the free MSPs is $k \sim 2.5$. However, in the distributions derived from MUDD, we obtain exponents of $k \sim 3.3 \pm 0.7$ for $P_c \propto r^2$ and $k \sim 3.7 \pm 0.5$ for $P_c \propto r^3$ for MXD-1, and $k \sim 3.6 \pm 0.8$ and $k \sim 4.4 \pm 0.3$ for MXD-1B, where the errors are based on the 95% prediction bounds. These values ($k \gtrsim 3$; Evans, 1994) may indicate that the distribution of the fragments reaching the bottom plate has not changed significantly from G2. Such a result may not agree with earlier work (Antonsen & Havnes, 2015) that indicate that only MSPs survive, and that the initial fragment distribution created in the collision with G2 changes toward lower k values as a result of fragment evaporation. From experiments, it has been found that ice particles $\lesssim$ 7 nm have a charging probability $\propto m^{3/2}$, and small water ice grains are found to stick effectively to metal surfaces (Tomsic, 2001). Moreover, very small ice grains that will also thermalize evaporate rapidly, according to extensive modeling of fragment dynamics and evaporation (Antonsen & Havnes, 2015). In that case, the inverse power law will be stronger than the one for pure MSPs and will probably have a cutoff and deviate from an ideal inverse power scaling. This makes ice particles an unlikely candidate to dominate the size distribution. We must also note that the uncertainties are many, and the inverse power law obtained here is nothing more than indicative of the expected size distribution. A significant source of error in the fitted distribution may lie in the determination of the sizes in the attracting potential mode, as dynamics of such small grains are difficult to simulate reliably. If the sizes from the smallest potential bins were shifted up only a few Ångstrøms, then the resulting size distribution would follow a significantly weaker inverse power law.

5. Discussion

We have in this work presented measurements from two triplets of the Faraday bucket probe MUDD launched on the MaxiDusty payloads MXD-1 and MXD-1B in the summer of 2016. In principle, the probes provide a simple technique to analyze the fragments of mesospheric ice particles larger than ~10 nm and are expected to separate between signatures of pure ice and meteoric agglomerates contained inside the particles entering the probes. From the combined measurements of the three probes and through numerical simulations of dust movement inside them (see Antonsen & Havnes, 2015), we have derived two 10-point size distributions of collision fragments. The size distributions can be fitted by inverse power laws. From considerations of fragment evaporation and dynamics, we find it unlikely that the measured currents are from pure ice, and thus, the derived size distribution should reflect the one of the MSPs. The exponents of the obtained power laws, $k \sim [3.3 \pm 0.7, 3.7 \pm 0.5]$ and $k \sim [3.6 \pm 0.8, 4.4 \pm 0.3]$ for the two flights, respectively, show as expected from theory (Hunten et al., 1980; Megner et al., 2006) and measurements of an earlier version of MUDD (Havnes et al., 2014) that the number of fragments of sizes around a few Ångstrøms, assumably MSPs, is at least 1 order of magnitude larger than the number of $\sim$ 1 nm particles. The obtained distribution would, by these arguments, be dominated by MSPs embedded in the ice particles. The power laws should not, however, be utilized as the size distribution of free MSPs as the growth and fragmentation process might also affect the distribution. Havnes et al. (2014) and Antonsen and Havnes (2015) discussed the possibility of larger ice fragments "disguising" as MSPs as a possible source of error. Another uncertainty in deriving the size distributions lies in the fragment charging and especially the triboelectric charging, which is thought to be dominant for nanometer size dust particles in the fragmentation process.

To provide additional justification for our conclusions, we can estimate the volume filling factor of presumable MSPs inside the NLC particles. The volume filling factor is a measurement of the content by volume of meteoric material in the ice particles. Following Havnes et al. (2014), the collected current on the bottom plate can be expressed as $I_{BP} = \xi N_d e A_M v_R$, where ξ is the number of charged fragments produced in a single

particle collision with G2, N_d is the number density of ice particles, $A_M = \pi \cdot 0.045^2$ m^2 is the MUDD cross section, $e = 1.6 \cdot 10^{-19}$ C is the elementary charge, and $v_R = 800$ m s^{-1} is the rocket velocity. For a simple estimate of ξ, we use values from MXD-1 at ~ 85 km. Inserting for the MUDD current, $|I_{BP}| = 1$ nA, we obtain $\xi N_d = 1.23\times10^9$m^{-3}. The charge number density, shown in Figure 16 for MXD-1, was obtained from measurements with the Faraday cup probe DUSTY and can be found in Figure 16 to be $|N_d Z_d| \approx 1.5\times10^9$ m^{-3}, where Z_d is the charge number of ice particles (typically $\bar{Z}_d = -1$ or a few times this in very active regions). Furthermore, assuming that monodispersive NLC particles with radii of 15 nm and concentration N_{15} produced the electron bite-out while a population of particles with radii 50 nm and concentration N_{50} produced the optical scattering, we can estimate that the measured charge number density was produced by ice particle concentrations of $N_{15} \approx 10^9$ m^{-3} and $N_{50} \approx 5\times10^7$ m^{-3} by using realistic charge distributions. We are then left with the equation $N_{50}\xi + N_{15}\xi(15/50)^3 = 1.23 \times 10^9$ m^{-3} that yields $\xi = 16$. The volume filling factor is dependent on the MSP size distribution; but for a homogeneous example population of 0.9 nm particles, the volume filing factor becomes $\approx 16 \times (0.9/50)^3 \times 100\% = 0.01\%$ for an ice particle with radius 50 nm and $\approx 0.075\%$ for a 25 nm ice particle. This is of course for the case when all fragments are charged, so that the actual filling factor can probably be at least 1 order of magnitude larger when accounting for charging probabilities. If assuming that all fragments are pure ice and accounting for their charging probability, we obtain unphysical filling factors of > 100%. This feature agrees well with the findings of Hervig et al. (2012) who found filling factors within the range 0.01–3% and Havnes et al. (2014) (for the first flight of MUDD on the PHOCUS payload) where the conclusion was that MSPs are abundant inside NLC particles with filling factors between 0.05% and several percent.

Acknowledgments
The MAXIDUSTY rocket campaign with related research was supported by the Norwegian Research Council and the Norwegian Space Centre. We would also like to thank Ralph Latteck and Gerd Baumgarten at IAP for providing MAARSY radar data and RMR lidar data, respectively, and Martin Friedrich for providing electron density data. All data related to MUDD, as well as raw data for all instruments, are available from the UiT Open Research repository at https://dataverse.no/dataset.xhtml?persistentId=doi:10.18710/KSGADN or through the DOI identifier. Raw PCM data from all instruments are also available from Andøya Space Center.

References

Adams, N. G., & Smith, D. (1971). Studies of microparticle impact phenomena leading to the development of a highly sensitive micrometeoroid detector. *Planetary and Space Science*, *19*(2), 195–204. https://doi.org10.1016/0032-0633(71) 90199-1

Antonsen, T., & Havnes, O. (2015). On the detection of mesospheric meteoric smoke particles embedded in noctilucent cloud particles with rocket-borne dust probes. *Review of Scientific Instruments*, *86*(3), 033305. https://doi.org10.1063/1.4914394

Bardeen, C. G., Toon, O. B., Jensen, E. J., Marsh, D. R., & Harvey, V. L. (2008). Numerical simulations of the three-dimensional distribution of meteoric dust in the mesosphere and upper stratosphere. *Journal of Geophysical Research*, *113*, D17202. https://doi.org10.1029/2007JD009515

Baumgarten, G., Fiedler, J., Lübken, F.-J., & von Cossart, G. (2008). Particle properties and water content of noctilucent clouds and their interannual variation. *Journal of Geophysical Research*, *113*, D06203. https://doi.org10.1029/2007JD008884

Bekkeng, T. A., Jacobsen, K. S., Bekkeng, J. K., Pedersen, A., Lindem, T., Lebreton, J. P., & Moen, J. I. (2010). Design of a multi-needle Langmuir probe system. *Measurement Science and Technology*, *21*(8), 085903.

Evans, A. (1994). *The dusty universe*, Series in Astronomy. Chichester, New York: John Wiley.

Friichtenicht, J. F. (1964). Micrometeoroid simulation using nuclear accelerator techniques. *Nuclear Instruments and Methods*, *28*(1), 70–78. https://doi.org10.1016/0029-554X(64)90351-9

Gerding, M., Kopp, M., Höffner, J., Baumgarten, K., & Lübken, F.-J. (2016). Mesospheric temperature soundings with the new, daylight-capable IAP RMR lidar. *Atmospheric Measurement Techniques*, *9*(8), 3707–3715. https://doi.org10.5194/amt-9-3707-2016

Gumbel, J., & Megner, L. (2009). Charged meteoric smoke as ice nuclei in the mesosphere: Part 1—A review of basic concepts. *Journal of Atmospheric and Solar-Terrestrial Physics*, *71*(12), 1225–1235.

Havnes, O., & Hartquist, T. W. (2016). Nanodust shedding and its potential influence on dust-related phenomena in the mesosphere. *Journal of Geophysical Research: Atmospheres*, *121*, 12,363–12,376. https://doi.org10.1002/2016JD025037

Havnes, O., & Næsheim, L. I. (2007). On the secondary charging effects and structure of mesospheric dust particles impacting on rocket probes. *Annales Geophysicae*, *25*(3), 623–637. https://doi.org10.5194/angeo-25-623-2007

Havnes, O., Trøim, J., Blix, T., Mortensen, W., Næsheim, L. I., Thrane, E., & Tønnesen, T. (1996). First detection of charged dust particles in the Earth's mesosphere. *Journal of Geophysical Research*, *101*(A5), 10,839–10,847. https://doi.org10.1029/96JA00003

Havnes, O., Gumbel, J., Antonsen, T., Hedin, J., & Hoz, C. La (2014). On the size distribution of collision fragments of NLC dust particles and their relevance to meteoric smoke particles. *Journal of Atmospheric and Solar-Terrestrial Physics*, *118*, 190–198. https://doi.org10.1016/j.jastp.2014.03.008

Havnes, O., Antonsen, T., Hartquist, T. W., Fredriksen, Å., & Plane, J. M. C. (2015). The Tromsø programme of in situ and sample return studies of mesospheric nanoparticles. *Journal of Atmospheric and Solar-Terrestrial Physics*, *127*, 129–136. https://doi.org10.1016/j.jastp.2014.09.010

Hedin, J., Gumbel, J., & Rapp, M. (2007). On the efficiency of rocket-borne particle detection in the mesosphere. *Atmospheric Chemistry and Physics*, *7*(14), 3701–3711. https://doi.org10.5194/acp-7-3701-2007

Hervig, M., McHugh, M., & Summers, M. E. (2003). Water vapor enhancement in the polar summer mesosphere and its relationship to polar mesospheric clouds. *Geophysical Research Letters*, *30*(20), 2041. https://doi.org10.1029/2003GL018089

Hervig, M. E., Deaver, L. E., Bardeen, C. G., Russell, J. M. III, Bailey, S. M., & Gordley, L. L. (2012). The content and composition of meteoric smoke in mesospheric ice particles from SOFIE observations. *Journal of Atmospheric and Solar-Terrestrial Physics*, *84-85*, 1–6. https://doi.org10.1016/j.jastp.2012.04.005

Hunten, D. M., Turco, R. P., & Toon, O. B. (1980). Smoke and dust particles of meteoric origin in the mesosphere and stratosphere. *Journal of the Atmospheric Sciences*, *37*(6), 1342–1357. https://doi.org10.1175/1520-0469(1980)037<1342:SADPOM>2.0.CO;2

Jacobsen, K. S., Pedersen, A., Moen, J. I., & Bekkeng, T. A. (2010). A new Langmuir probe concept for rapid sampling of space plasma electron density. *Measurement Science and Technology*, *21*(8), 085902.

Jacobsen, T. A, & Friedrich, M. (1979). Electron density measurements in the lower *D*-region. *Journal of Atmospheric and Terrestrial Physics*, *41*(12), 1195–1200. https://doi.org10.1016/0021-9169(79)90022-9

Kassa, M., Rapp, M., Hartquist, T. W., & Havnes, O. (2012). Secondary charging effects due to icy dust particle impacts on rocket payloads. *Annales Geophysicae*, *30*(3), 433–439. https://doi.org10.5194/angeo-30-433-2012

Klekociuk, A. R., Brown, P. G., Pack, D. W., ReVelle, D. O., Edwards, W. N., Spalding, R. E., … Zagari, J. (2005). Meteoritic dust from the atmospheric disintegration of a large meteoroid. *Nature*, *436*(7054), 1132–1135. https://doi.org10.1038/nature03881

Knappmiller, S., Rapp, M., Robertson, S., & Gumbel, J. (2011). Charging of meteoric smoke and ice particles in the mesosphere including photoemission and photodetachment rates. *Journal of Atmospheric and Solar-Terrestrial Physics*, *73*(14–15), 2212–2220. https://doi.org10.1016/j.jastp.2011.01.008

Kuuluvainen, H., Arffman, A., Saukko, E., Virtanen, A., & Keskinen, J. (2013). A new method for characterizing the bounce and charge transfer properties of nanoparticles. *Journal of Aerosol Science*, *55*, 104–115. https://doi.org10.1016/j.jaerosci.2012.08.007

Lübken, F-J. (1999). Thermal structure of the arctic summer mesosphere. *Journal of Geophysical Research*, *104*(D8), 9135–9149.

Megner, L., Rapp, M., & Gumbel, J. (2006). Distribution of meteoric smoke—Sensitivity to microphysical properties and atmospheric conditions. *Atmospheric Chemistry and Physics*, *6*(12), 4415–4426. https://doi.org10.5194/ acp-6-4415-2006

Murray, B. J., & Jensen, E. J. (2010). Homogeneous nucleation of amorphous solid water particles in the upper mesosphere. *Journal of Atmospheric and Solar-Terrestrial Physics*, *72*(1), 51–61. https://doi.org10.1016/j.jastp. 2009.10.007

Plane, J. M. C. (2003). Atmospheric chemistry of meteoric metals. *Chemical Reviews*, *103*(12), 4963–4984. https://doi.org10.1021/cr0205309

Plane, J. M. C. (2011). On the role of metal silicate molecules as ice nuclei. *Journal of Atmospheric and Solar-Terrestrial Physics*, *73*(14–15), 2192–2200. https://doi.org10.1016/j.jastp.2010.07.008

Rapp, M., & Lübken, F.-J. (2004). Polar mesosphere summer echoes (PMSE): Review of observations and current understanding. *Atmospheric Chemistry and Physics*, *4*(11/12), 2601–2633. https://doi.org10.5194/acp-4-2601-2004

Rapp, M., & Thomas, G. E. (2006). Modeling the microphysics of mesospheric ice particles: Assessment of current capabilities and basic sensitivities. *Journal of Atmospheric and Solar-Terrestrial Physics*, *68*(7), 715–744.

Reid, G. C. (1997). The nucleation and growth of ice particles in the upper mesosphere. *Advances in Space Research*, *20*(6), 1285–1291. https://doi.org10.1016/S0273-1177(97)00788-6

Robertson, S., Horanyi, M., Knappmiller, S., Sternovsky, Z., Holzworth, R., Shimogawa, M., … Hervig, M. E. (2009). Mass analysis of charged aerosol particles in NLC and PMSE during the ECOMA/MASS campaign. *Annales Geophysicae*, *27*(3), 1213–1232. https://doi.org10.5194/angeo-27-1213-2009

Tomsic, A. (2001). Collisions between water clusters and surfaces (PhD thesis), Göteborg University, Gothenburg, Sweden.

von Cossart, G., Fiedler, J., & von Zahn, U. (1999). Size distributions of NLC particles as determined from 3-color observations of NLC by ground-based lidar. *Geophysical Research Letters*, *26*, 1513–1516. https://doi.org10.1029/1999GL900226

Von Zahn, U., Von Cossart, G., Fiedler, J., Fricke, K. H., Nelke, G., Baumgarten, G., … Adolfsen, K. (2000). The ALOMAR Rayleigh/Mie/Raman lidar: Objectives, configuration, and performance. *Annales Geophysicae*, *18*(7), 815–833.

Zahn, U., & Meyer, W. (1989). Mesopause temperatures in polar summer. *Journal of Geophysical Research*, *94*(D12), 14,647–14,651.

Zasetsky, A. Y., Petelina, S. V., & Svishchev, I. M. (2009). Thermodynamics of homogeneous nucleation of ice particles in the polar summer mesosphere. *Atmospheric Chemistry and Physics*, *9*(3), 965–971. https://doi.org10.5194/acp-9-965-2009